

Stereolithography-Derived Three-Dimensional Pyrolytic Carbon/ Mn_3O_4 Nanostructures for Free-Standing Hybrid Supercapacitor Electrodes

Babak Rezaei, Thomas Willum Hansen, and Stephan Sylvest Keller*

Cite This: *ACS Appl. Nano Mater.* 2022, 5, 1808–1819

Read Online

ACCESS |

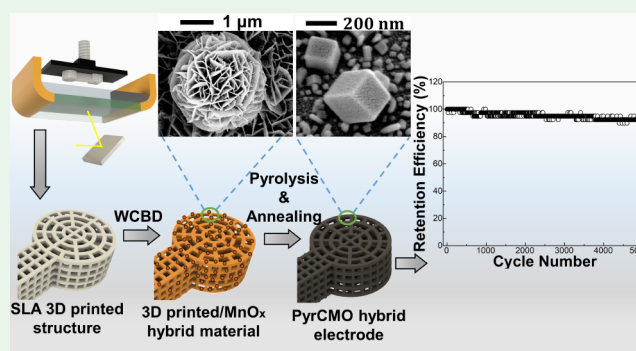
Metrics & More

Article Recommendations

Supporting Information

ABSTRACT: The development of permeable three-dimensional (3D) macroporous carbon architectures loaded with active pseudocapacitive nanomaterials offers hybrid supercapacitor (SC) materials with higher energy density, shortened diffusion length for ions, and higher charge–discharge rate capability and thereby is highly relevant for electrical energy storage (EES). Herein, structurally complex and tailorable 3D pyrolytic carbon/ Mn_3O_4 hybrid SC electrode materials are synthesized through the self-assembly of MnO_2 nanoflakes and nanoflowers onto the surface of stereolithography 3D-printed architectures via a facile wet chemical deposition route, followed by a single thermal treatment. Thermal annealing of the MnO_2 nanostructures concurrent with carbonization of the polymer precursor leads to the formation of a 3D hybrid SC electrode material with unique structural integrity and uniformity. The microstructural and chemical characterization of the hybrid electrode reveals the predominant formation of crystalline hausmannite- Mn_3O_4 after the pyrolysis/annealing process, which is a favorable pseudocapacitive material for EES. With the combination of the 3D free-standing carbon architecture and self-assembled binder-free Mn_3O_4 nanostructures, electrochemical capacitive charge storage with very good rate capability, gravimetric and areal capacitances (186 F g^{-1} and 968 mF cm^{-2} , respectively), and a long lifespan ($>92\%$ after 5000 cycles) is demonstrated. It is worth noting that the gravimetric capacitance value is obtained by considering the full mass of the electrode including the carbon current collector. When only the mass of the pseudocapacitive nanomaterial is considered, a capacitance value of 457 F g^{-1} is achieved, which is comparable to state-of-the-art Mn_3O_4 -based SC electrode materials.

KEYWORDS: additive manufacturing, pseudocapacitive nanomaterial, hybrid supercapacitor material, stereolithography, self-assembly, free-standing electrodes



1. INTRODUCTION

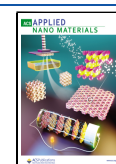
The development of hierarchically organized porous nanomaterials with modular structures is an area of considerable research interest in diverse applications ranging from catalysis to sensing.^{1,2} As a consequence of the steadily growing demand for electrical energy storage (EES) for portable electronic devices, the development and discovery of high-performance and small-scale energy storage materials have aroused considerable attention.³ Driven by the need for EES, a variety of technologies, such as batteries, fuel cells, and electrochemical capacitors, with different charge storage mechanisms and performance characteristics have been developed.⁴ Among them, electrochemical capacitors, often referred to as supercapacitors (SCs), have emerged as highly competitive energy storage devices providing high power density, rapid charge–discharge rate, low maintenance cost, and long cycle life.^{5,6} Depending on the mechanism of charge storage and the types of electrode materials, SCs can be divided into two major categories: electric double-layer capacitors (EDLCs) and pseudocapacitors.^{3,7} In

EDLCs, pure electrostatic charge is accumulated through physical adsorption and desorption (non-Faradaic reactions) of electrolyte ions on the high surface area of carbonaceous materials. In comparison, pseudocapacitors store charge via fast and reversible electrochemical redox reactions (Faradaic reactions) at the surface or in the first few tens of nanometers of the bulk of transition-metal oxides/sulfides and conducting polymers.^{8,9} Although these materials have proven to be useful and promising for EES, they also suffer from some intrinsic drawbacks, such as low energy density for EDLCs and poor cycle life for pseudocapacitors. More recently, remarkable efforts have

Received: October 5, 2021

Accepted: December 1, 2021

Published: December 20, 2021



been undertaken to address these limitations by exploring the respective advantages of carbonaceous and pseudocapacitive materials, obtaining novel hybrid SC materials. Here the former are able to provide a high energy density, while the latter can effectively improve the electrode capacitance.^{10,11} Moreover, it has been shown that this combination results in synergistic effects, further improving the performance.¹² Carbon-based materials are widely employed not only in hybrid SC materials because of their electric double-layer contribution to the overall capacitance but also as an electron current collectors because of their outstanding electrical conductivity, large specific surface area, and cycle stability.

Different combinations of pseudocapacitive materials, such as RuO₂, NiO, Co₃O₄, Ni(OH)₂, MnO_x, V₂O₅, polythiophenes, polyaniline, and polypyrrole, and carbonaceous materials have been extensively studied for the development of hybrid SC materials. Of these, MnO_x-based hybrid SCs are particularly attractive because MnO_x possesses the prominent advantages of high theoretical specific capacitance, natural abundance, environmental compatibility, and low cost.^{8,10} Among the various oxidation states of MnO_x, lower valence states such as Mn₂O₃ and Mn₃O₄ are known as the most favorable materials for EES because of (i) the higher stability of these oxidation states, which is crucial for long-term performance and good corrosion stability, (ii) the redox reaction of manganese ions in these oxidation states occurring spontaneously during the charge–discharge process, and (iii) their relatively broad work potential window in aqueous electrolyte solutions.^{13–16} To apply various MnO_x nanostructures synthesized by different methods, such as solvothermal, hydrothermal, sonochemical, and sol–gel, to the surface of the electrodes, these are usually combined with a conductive agent and a polymer binder [poly(vinylidene fluoride), poly(tetrafluoroethylene), or Nafion] in a paste. This paste is cast and dried onto the surface of a conductive current collector or substrate (e.g., aluminum, stainless steel sheets, silicon wafer, etc.). The overall capacitances of the resulting hybrid electrodes are typically higher than those of the bare substrates. However, they are considerably lower than the theoretically estimated values because of (i) the indirect electrical connection of the nanoparticles and the electrode surface, (ii) the internal resistance of the polymer binder, and (iii) the significant contribution of the employed paste on the overall mass of the SC electrode.^{10,17,18} More recently, some binder-free approaches have been developed based on the *in situ* synthesis and direct decoration of the electrode surface with MnO₂ nanostructures, such as chemical vapor deposition and electrochemical deposition methods.¹⁹ The direct decoration of the electrode surface with MnO₂ nanostructures offers great promise for producing high-performance hybrid SC electrodes. However, a postannealing treatment is required to remove the intercalated ions, enhance the crystallization of the particles, and improve the integrity of the nanostructured layer deposited on the electrode surface.^{20,21}

The electrochemical behavior of the SC electrodes strongly relies on their physicochemical characteristics such as the surface area, structural integrity, electrical conductivity, wettability of the electrode surface with an electrolyte, and permeability of the electrolyte solution.⁷ Besides these factors, the overall electrochemical performance of the SC is also largely dependent on the morphology and architecture of the electrode materials.²² In this regard, employing permeable three-dimensional (3D) architectures loaded with active material offers

higher energy density, shortened diffusion length for the ions, and higher charge–discharge rate capability compared with the same footprint area of 2D materials.^{5,23,24} Therefore, recent efforts have been directed toward constructing novel 3D electrode architectures by various microfabrication techniques such as photolithography,^{9,25} an elastocapillary self-assembly process,²⁶ or deep reactive ion etching combined with photolithography.²⁷ However, the construction of structurally complex and tailorable hierarchical SC electrodes with these methods is challenging because of the inherent process limitations for the fabrication of more complex 3D architectures and the expensive and time-consuming procedures.^{5,28} Therefore, more facile, cost-effective, and innovative fabrication techniques are required to achieve structurally complex and tailorable 3D carbon electrodes for energy storage in SCs.

Here, we report for the first time a simple, yet versatile approach for the fabrication of 3D hierarchical hybrid SC electrodes by the self-assembly of MnO_x nanostructures onto the surface of stereolithography (SLA) 3D-printed polymer precursor structures via a wet chemical deposition route, followed by a pyrolysis process. Carbonization of the 3D polymer network and annealing of the metal oxide nanomaterial on its surface occurred concurrently in a single thermal processing step in an inert atmosphere. Simultaneous annealing/pyrolysis contributes to the high structural integrity and stability of the electrodes and thereby provides excellent electrical contact between the MnO_x nanostructures and the carbon and enhances the electron transport/collection. The hybrid SC electrode developed in this research is (i) binder-free, (ii) self-supported, with the very lightweight 3D pyrolytic carbon (PyrC) structure itself acting as a current collector, (iii) free-standing, meaning that no additional substrate is needed, and (iv) permeable for ions and electrolytes because of their specific open design. With the novel combination of hierarchical MnO_x nanostructures and a SLA-derived 3D complex carbon architecture, a free-standing hybrid SC electrode with good rate capability, high gravimetric and areal capacitances (186 F g⁻¹ and 968 mF cm⁻², respectively), and capacitance retention of 92.3% after 5000 cycles is obtained. Moreover, the MnO_x nanomaterial itself showed a specific capacitance value of 457 F g⁻¹ at a current density of 0.5 mA cm⁻². We are convinced that the introduced approach opens new avenues to design tailorable 3D hybrid SC electrodes for energy storage.

2. EXPERIMENTAL APPROACH

In previous work, a commercial photopolymer (Formlabs high-temperature resin, HTR), composed of acrylated monomers and methacrylated oligomers,²⁹ was employed to print complex 3D structures and identified as pyrolyzable material.³⁰ More details about the physicochemical properties of the commercial photopolymer resin utilized in this research are summarized in Table S1. For fabrication of the complex 3D polymer precursor structures, 3D models were designed using Fusion360 software and directly SLA-printed (support-free printing) on the surface of a 6-in. silicon wafer mounted on the printer platform. Support-free printing on the smooth silicon substrate contributes to the improved uniformity and repeatability of the 3D-printed structures. A further postcuring process was carried out for 2 h in an UV exposure chamber (wavelength of 405 nm, BSL-01, Opsytec Dr. Gröbel, Germany) to enhance the cross-linking efficiency and strength of the polymer network. The postcured 3D-printed structures were utilized as the substrates for the subsequent deposition of MnO_x nanoflakes and nanoflowers via a facile one-step wet chemical reduction of manganese salt in a HCl solution. Briefly, a measured amount of KMnO₄ (1.25, 2.5, 5, and 10 mM) was dissolved in 25 mL of a 0.01 M HCl solution and transferred to a 100 mL round-bottom flask equipped

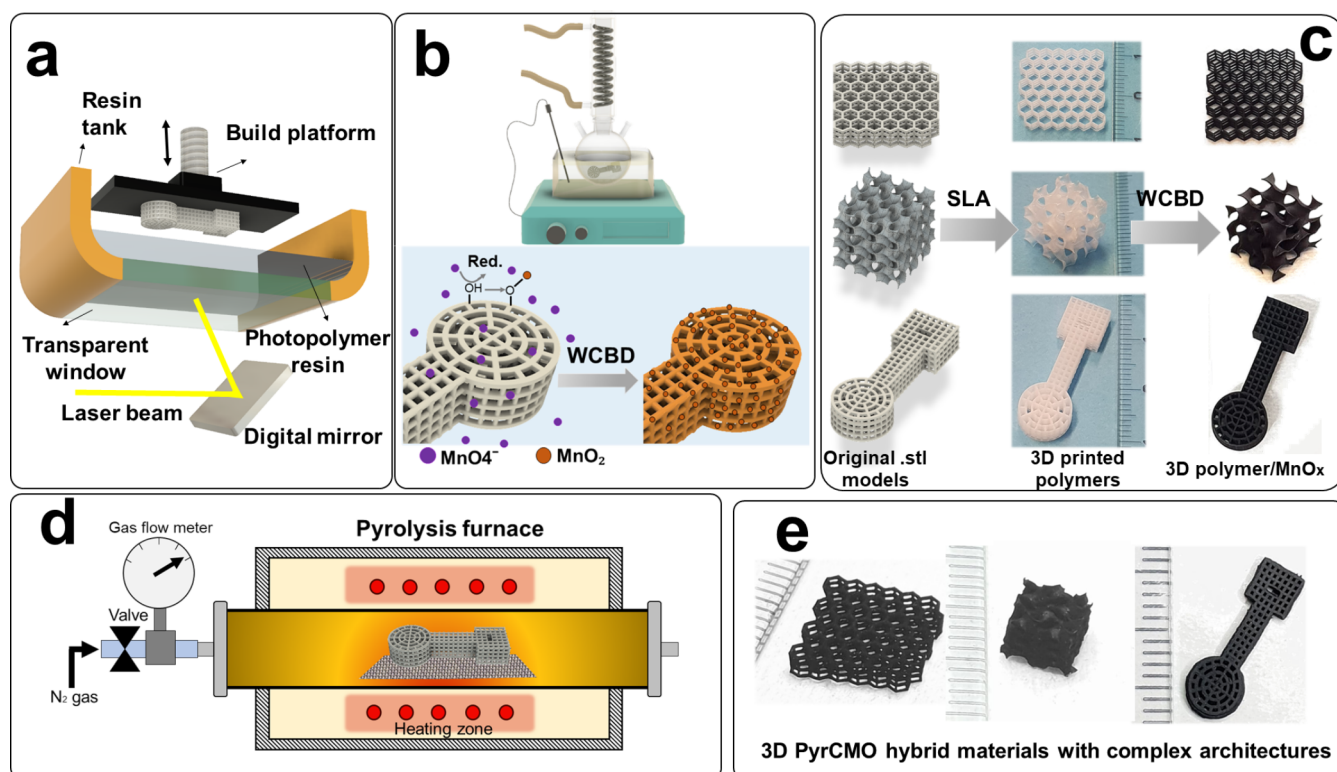


Figure 1. Schematic illustrations: (a) SLA 3D-printing procedure to generate a 3D free-standing reticular configuration of a pyrolyzable photopolymer resin. (b) Synthesis and self-assembly of the MnO_2 nanostructures onto the surface of the 3D-printed polymer network through the WCBD method. (c) Original .stl models of the honeycomb, gyroid, and reticular geometries and digital photographs of their SLA 3D prints before and after decoration with MnO_x . (d) Pyrolysis/annealing process of the 3D-printed polymer/ MnO_2 hybrid materials in a ceramic tube furnace with a piece of stainless steel sheet to increase the uniformity of thermal degradation and gas evolution. (e) Digital photograph of the 3D PyrCMO hybrid electrode with different geometries.

with a heating oil bath, a magnetic stirrer, and a reflux condenser. Prior to transferring the 3D-printed object to the flask, it was exposed to oxygen plasma (Zepto, Diener plasma surface technology, Germany) for 60 s to boost its wettability in the metal oxide precursor solution. The mixture was heated to reflux at boiling temperature for 4 h. After cooling to room temperature, the sample was removed from the flask, rinsed gently three times with deionized water to remove the excess of weakly bound particles, and dried under ambient conditions overnight. Afterward, carbonization of the polymer network, annealing, and purification of the MnO_x nanostructures decorated on the surface of the 3D-printed sample were conducted simultaneously in a single thermal process in a horizontal tube furnace (MTI Corp., GSL 1700x) under a nitrogen gas flow (200 sccm). In order to obtain an effective and uniform gasification condition during the carbonization process, the sample was placed in a stainless steel mesh boat. The boat, located inside the furnace, was heated at $2\text{ }^\circ\text{C min}^{-1}$ to $450\text{ }^\circ\text{C}$ and then at $3\text{ }^\circ\text{C min}^{-1}$ up to $900\text{ }^\circ\text{C}$ and kept at $900\text{ }^\circ\text{C}$ for 5 h. Next, the furnace was cooled to room temperature under a nitrogen gas flow.

The morphology and surface topography of the MnO_x nanostructures decorated on the surface of the SLA 3D-printed samples before and after the pyrolysis/annealing process were evaluated by scanning electron microscopy (SEM; Zeiss Supra VP 40, Germany). *ImageJ* software (National Institute of Health, USA) was used to estimate the average thickness and diameter of the MnO_x nanoflakes and nanoparticles, respectively. X-ray diffraction (XRD) spectra of the samples were obtained using PANalytical model AERIS X-ray diffractometer (Malvern Panalytical Ltd., Almedo, The Netherlands) with $\text{Cu K}\alpha$ radiation ($\lambda = 1.5406\text{ \AA}$, voltage = 40 kV, and beam current = 30 mA). X-ray photoelectron spectroscopy (XPS; Thermo Scientific Nexsa, USA) and energy-dispersive X-ray spectrometry (EDS; FEI Quanta FEG 200 ESEM scanning electron microscope equipped with an Oxford X Max EDS detector) were employed for analysis of the elemental composition and chemical states of the synthesized samples

before and after thermal treatment. Raman spectroscopy was conducted using a micro-Raman system (Thermo Scientific Nexsa, USA) with a laser wavelength of 532 nm. High-resolution transmission electron microscopy (HRTEM) was carried out in an FEI Tecnai T20 transmission electron microscope. The samples were prepared by grinding the as-synthesized PyrCMO with ethanol and drop-casting the powder–ethanol suspension on a gold grid with a carbon support film.

The electrochemical studies were conducted in a 10 mL three-electrode electrochemical cell comprising an Ag/AgCl electrode as the reference electrode, a $10\text{ mm} \times 20\text{ mm}$ piece of silicon wafer on which both sides are coated with a platinum thin film (200 nm thickness; physical vapor deposition coating method) as the counter electrode, and 3D PyrCMO as the working electrode. The circular part of the electrode (effective area $\sim 0.96\text{ cm}^2$) was dipped into electrolyte solutions and then transferred to a vacuum chamber prior to electrochemical measurements to ensure effective infiltration of the electrolyte into the porous structure of the electrode. Electrochemical analysis of the PyrCMO electrodes was carried out by cyclic voltammetry (CV), galvanostatic charge–discharge (GCD) measurements, and electrochemical impedance spectroscopy (EIS) conducted on an Autolab PGSTAT128N potentiostat/galvanostat in combination with the NOVA program, version 2.1.4 (Metrohm Autolab BV, The Netherlands). The CV test was performed at the voltage range of -0.3 to $+0.8\text{ V}$ and different scan rates ranging from 2 to 100 mV s^{-1} . The GCD test was conducted at various current densities from 0.5 to 10 mA cm^{-2} and a voltage cutoff window of -0.3 to $+0.8\text{ V}$. EIS measurements were carried out with the same electrochemical cell and electrodes, at the corresponding open-circuit potential over a frequency range of 100 kHz to 10 mHz with a sinusoidal perturbation amplitude of 10 mV.

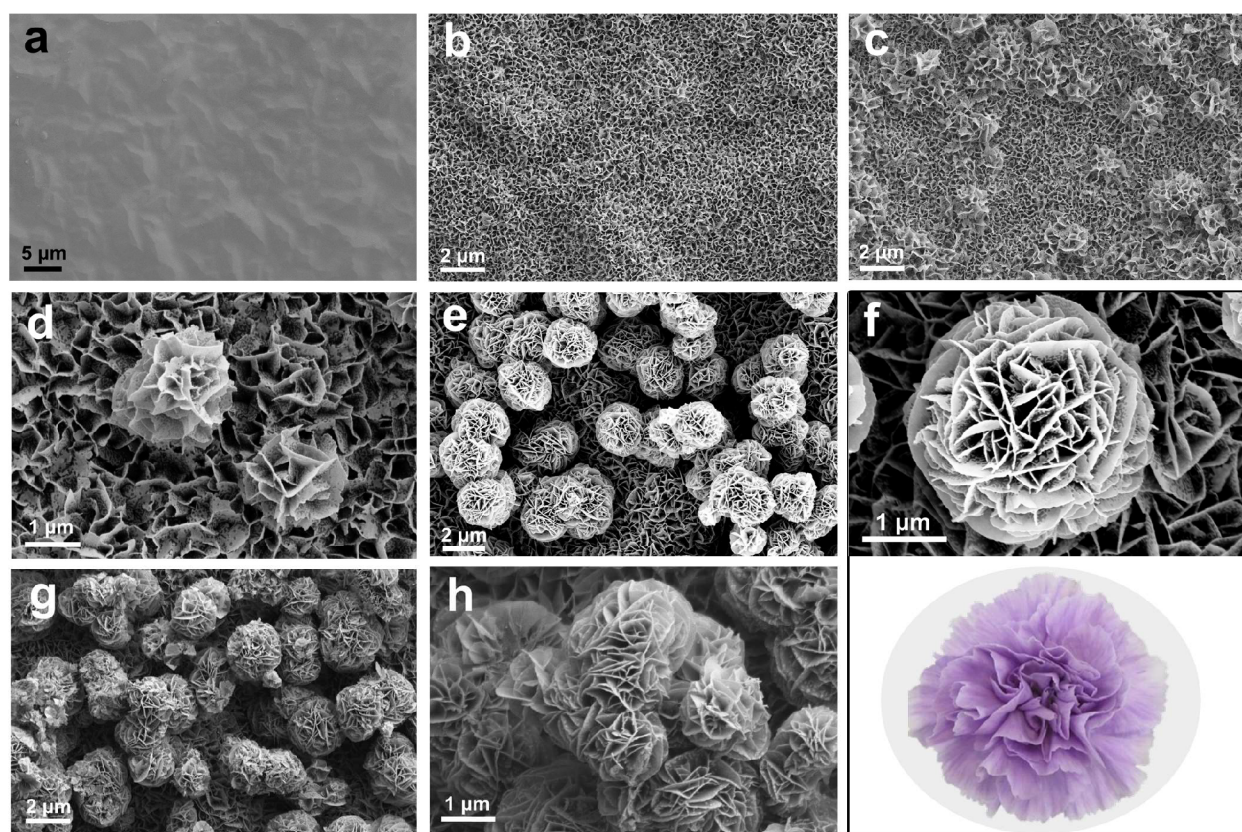


Figure 2. SEM images of (a) a bare 3D-printed polymer and 3D-printed polymer/ MnO_x hybrid materials obtained by using different MnO_x precursor concentrations of 1.25 mM (b) and 2.5 mM with low (c) and high (d) magnifications, 5 mM with low (e) and high (f) magnifications, and 10 mM with low (g) and high (h) magnifications.

3. RESULTS AND DISCUSSION

As schematically illustrated in Figure 1, first, free-standing 3D polymer precursor structures in a 3D reticular configuration were produced with SLA printing of a pyrolyzable resin (Figure 1a).³⁰ Figure 1b schematically shows the subsequent *in situ* synthesis of MnO_x nanostructures directly on the surface of the 3D-printed resin. Under very mild acidic conditions, a slow acidic reduction of potassium permanganate leads to the nucleation and self-assembly of nanostructures on the surface of the 3D-printed structure.^{20,31} The presence of oxygen-containing groups (e.g., hydroxyl and carboxyl groups) on the surface of the 3D-printed structure due to the chemical composition of the utilized photopolymer as well as the oxygen plasma treatment of the polymer surface prior to deposition renders it susceptible to oxidation and thereby decoration with a thin layer of MnO_x .^{12,32} The XPS spectra of the 3D-printed HTR before and after oxygen plasma treatment are shown in Figure S1a, and their elemental compositions are summarized in Table S2. As can be seen, the surface oxygen content increased from 19.8 to 28.6 atom % after plasma treatment, revealing the surface functionalization with oxygen-containing groups. Moreover, deconvolution of the high-resolution XPS spectra of C 1s (Figure S1b,c) indicates that the peak area ratios for C–O (hydroxyl and epoxy groups) at 285.8 eV, C=O (carbonyl group) at 286.7 eV, and O–C=O (carboxyl groups) at 289.2 eV increased after oxygen plasma treatment.^{33,34} These results further confirm the surface functionalization of the polymer with oxygen-containing groups through oxygen plasma exposure.

To demonstrate the capability of the developed approach to generate a 3D free-standing hybrid with various geometric

architectures, honeycomb, gyroid, and reticular patterns were designed, SLA 3D-printed, and chemically decorated with MnO_x , as shown in Figure 1c. As can be seen, the samples show excellent structural integrity and coating uniformity after wet chemical bath deposition (WCBD), regardless of the geometry of the 3D structures. The hybrid materials were heated at 900 °C under flowing N_2 to convert the 3D-printed polymer into a conductive 3D PyrC electrode (Figure 1d). Simultaneously, recrystallization and purification through inert-atmosphere annealing of the nanostructured MnO_x layer on the surface of the 3D-printed specimens lead to the formation of a PyrC/ MnO_x (PyrCMO) hybrid material with very good structural integrity and stability. The preservation of the 3D geometry and aspect ratios of different complex architectures during the pyrolysis/annealing treatment is illustrated in Figure 1e.

SEM images with different magnifications of the as-synthesized MnO_x nanostructures on the 3D-printed polymer precursor surface obtained by using different MnO_x precursor concentrations are shown in Figure 2. For a 1.25 mM KMnO_4 concentration, the 3D-printed polymer surface was completely decorated with an interconnected ultrathin nanoflake layer and displayed a rugged surface (Figure 2b). From the SEM images, the average thickness of the nanoflakes is found to be about 26 ± 8 nm. When the precursor concentration reached 2.5 mM, carnation flowerlike MnO_x (CFMnO_x) nanostructures composed of a cluster of leaves radiating from the middle were identified on the surface of the nanoflake structures (Figure 2c,d). It was also found that the CFMnO_x diameter increased when the metal oxide precursor concentration was further increased. A high-magnification SEM image of a single CFMnO_x

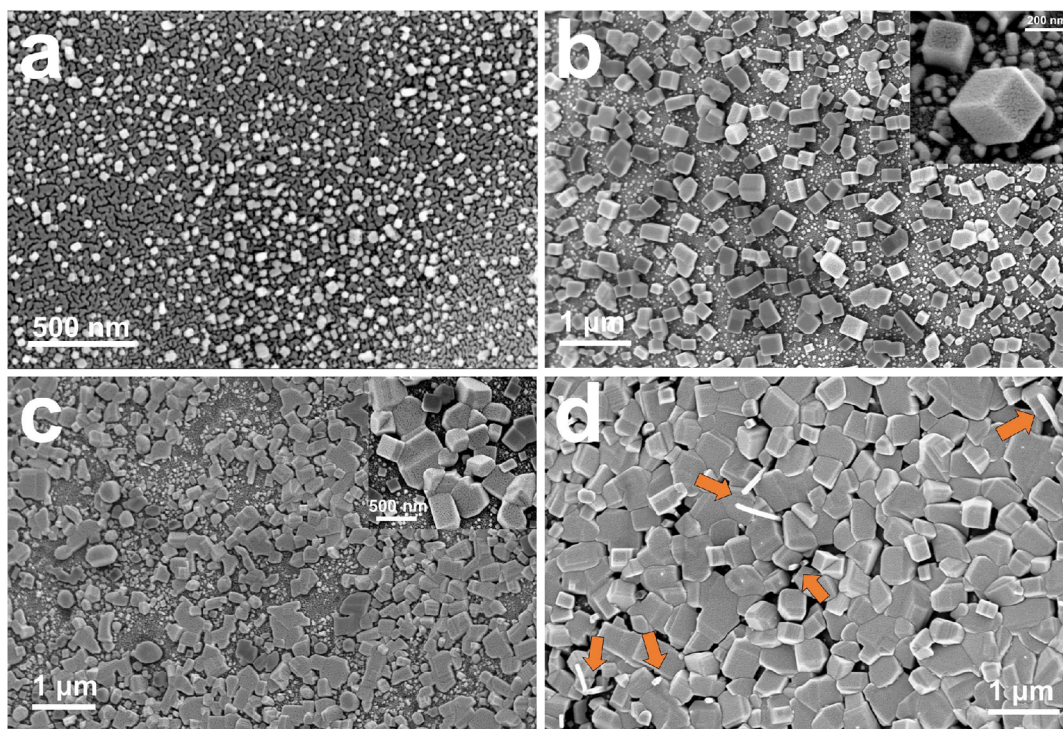


Figure 3. SEM images of the surface morphology of 3D PyrCMO hybrid electrodes after a pyrolysis/annealing process, fabricated with different metal oxide precursor concentrations of (a) 1.25, (b) 2.5, (c) 5, and (d) 10 mM.

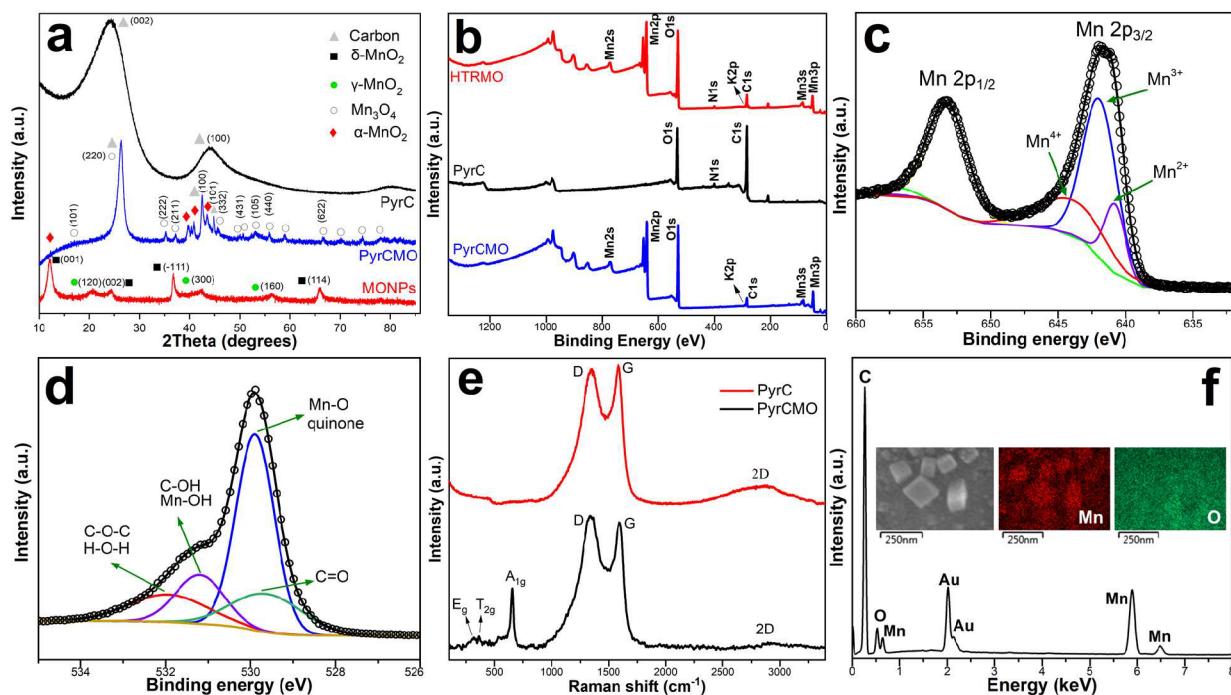


Figure 4. (a) XRD patterns of PyrC, PyrCMO, and MONP samples. (b) XPS survey spectra of the HTRMO, PyrC, and PyrCMO samples. High-resolution spectra for the Mn 2p (c) and O 1s (d) regions of the PyrCMO hybrid material. (e) Raman spectra of the PyrC and PyrCMO samples. (f) EDS spectrum, SEM image (inset left), and its corresponding elemental mappings of manganese (red) and oxygen (green) of the PyrCMO hybrid electrode.

nanostructure is presented in Figure 2f, illustrating the similarity of the synthesized structures with a real carnation flower (Figure 2f, bottom).

All of the samples were thermally treated in an inert environment at 900 °C to achieve (i) pyrolysis of the 3D-

printed polymer precursor and the fabrication of a 3D PyrC structure with complex and permeable architecture and (ii) purification, reorientation, and recrystallization of the MnO_x nanostructures decorating the surface of the 3D polymer structure.^{35–37} Kinetically, with a thermal annealing process,

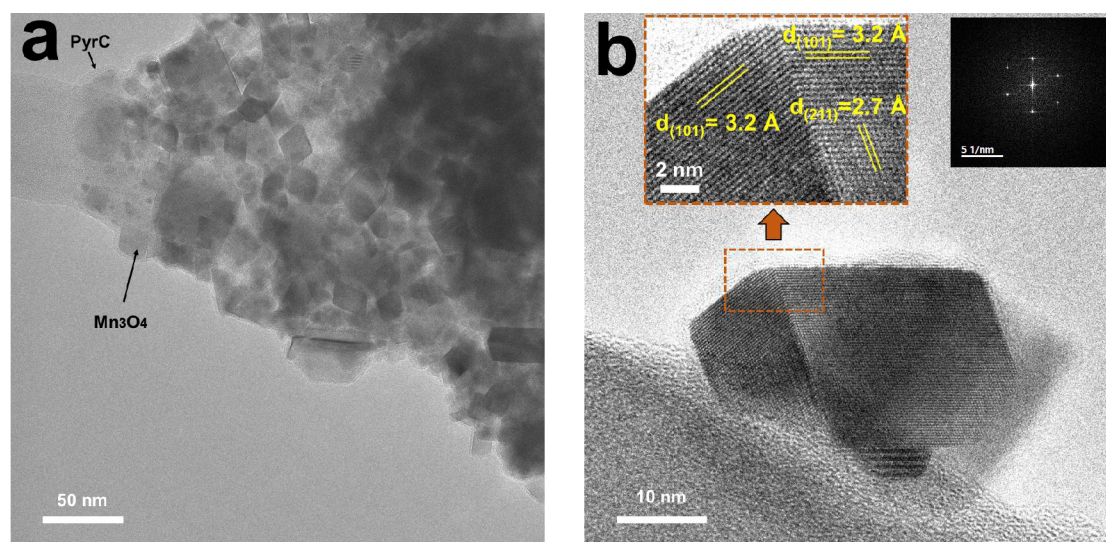


Figure 5. (a) TEM and (b) HRTEM images of the PyrCMO material with the corresponding FFT (inset) of the single-crystal Mn_3O_4 nanoparticle.

amorphous MnO_2 is first converted into crystalline MnO_2 , and a further increase of the annealing temperature results in the dissociation of crystalline MnO_2 into manganese oxide crystals with lower oxidation states.²⁰ It is known that the mentioned phase transformations are temperature-dependent, and different oxidation states could form by controlling the final annealing temperature.^{31,38} SEM images of the PyrCMO electrodes fabricated with different precursor concentrations are shown in Figure 3. As can be seen, after the thermal annealing process, a highly crystalline tetragonal structure of MnO_x is formed on the surface of a 3D PyrC. With an increase in the KMnO_4 concentration, the average size of the tetragonal particles increased and a more dense distribution of the nanoparticles was obtained. For instance, the average size of the nanoparticles increased from 36 ± 9 to 203 ± 46 nm as the metal oxide precursor concentration was raised from 1.25 to 2.5 mM. The high-magnification SEM image for the sample with a 2.5 mM precursor concentration (inset image of Figure 3b) reveals the formation of tiny rodlike nanoparticles concurrent with the formation of tetragonal metal oxide nanoparticles. Furthermore, for a 10 mM precursor concentration, a larger number of vertically grown nanorods was detected on the surface of the resulting PyrC materials (marked with arrows in Figure 3d).

For identification of the physicochemical reactions occurring during the thermal treatment, the chemical composition, phase purity, and crystal structures of the materials were assessed before and after the pyrolysis/annealing process using several analytical methods. Figure 4a shows the acquired powder XRD patterns for the as-synthesized MnO_x nanoparticles (MONPs), PyrC, and PyrCMO. The weak and broad diffraction peaks of the MONP could be ascribed to its poor crystalline properties. However, the clear characteristic peaks at 2θ of 12.3° , 24.4° , 36.6° , and 66.1° , indexing into the (001), (002), (-111), and (114) facets, respectively (JCPDS 80-1098), indicate that the birnessite-type manganese oxide ($\delta\text{-MnO}_2$) structure is synthesized.^{8,39} Moreover, the diffraction peaks at 2θ of 20.6° , 42.3° , and 56.3° may be attributed to the (120), (300), and (160) planes of $\gamma\text{-MnO}_2$, respectively (JCPDS 44-0412).⁴⁰ These results reveal that multiple crystalline phases are formed through the employed wet chemical deposition method. The XRD patterns of PyrC and PyrCMO exhibit two broad peaks around 25° and 43° , corresponding to the (002) and (100)

diffraction patterns of the pseudographitic carbon phases, respectively.⁴¹ For the PyrCMO sample, the (002) diffraction peak became narrower and moved to higher angles, which means that the graphene interlayer distance (d_{002}) decreased from 3.67 to 3.3 Å, indicating enhanced graphitization.⁴² The diffraction peaks of PyrCMO further reveal the presence of mixed phases of crystalline hausmannite- Mn_3O_4 (JCPDS 00-24-0734) and $\alpha\text{-MnO}_2$ (JCPDS 44-0141).^{38,43} The XPS survey spectra (Figure 4b) before and after the pyrolysis/annealing process confirm the presence of manganese atoms on the surface of the 3D-printed and carbon structures. The low atomic percentage of carbon (Table S3) on the surface of the high-temperature resin/ MnO_x (HTRMO) and PyrCMO indicate a uniform surface coating with MnO_x suppressing the background carbon signal. The XPS results also show the presence of potassium, which can be related to the formation of monoclinic potassium birnessite, constructed by the double chains of edge-sharing MnO_6 octahedral molecular layers separated from each other and stabilized with K^+ ions.^{8,40,44} The atomic percentage of the potassium element was found to increase with increasing precursor concentration (Figure S2a). The K^+ ion content has a profound effect on the morphology and phase conversion of manganese oxide during the annealing process and is known to act as a “growth director” in the formation of nanorods.^{20,39,45,46}

Therefore, the observed formation of more and longer nanorods for the samples with higher precursor concentrations (Figure 3d) could be ascribed to the higher number of intercalated K^+ ions within the structure. The high-resolution XPS spectra of Mn 2p and O 1s of PyrCMO are shown in parts c and d of Figure 4, respectively. Deconvolution of the Mn 2p_{3/2} peak into three peaks at the binding energies of 640.4 eV (Mn^{2+}), 641.8 eV (Mn^{3+}), and 643.9 eV (Mn^{4+}) reveals that the manganese exists in different valences and confirms the formation of multiple crystalline phases.^{20,47} Moreover, PyrCMO exhibited a separation energy of 5.5 eV for the Mn 3s doublet peaks (Figure S2b), suggesting that the predominant oxide phase is Mn_3O_4 ,^{3,48} which was further confirmed by XRD. Deconvolution of the O 1s peak (Figure 4d) reveals different states of oxygen atoms that chemically bond with carbon and manganese on the surface.³³

The crystalline structure of the annealed manganese oxide as well as the microcrystalline structure of PyrC was further investigated with Raman analysis. In the Raman spectrum shown

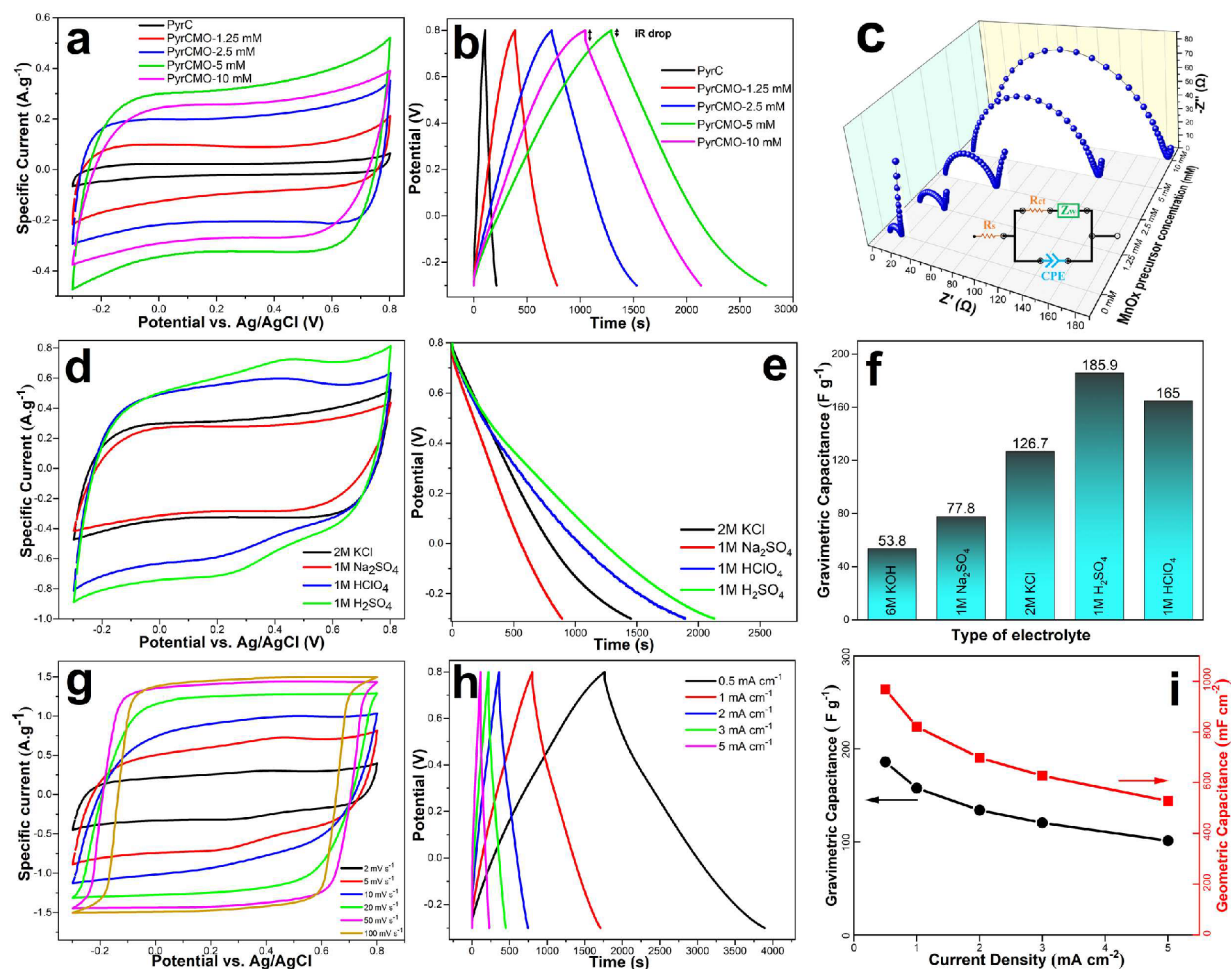


Figure 6. (a) CV curves at a scan rate of 5 mV s^{-1} , (b) GCD curves at a current density of 0.5 mA cm^{-2} , and (c) EIS results of the PyrC and PyrCMO hybrid electrodes prepared with different precursor concentrations, in a 2 M KCl solution as the electrolyte. (d) CV curves at a scan rate of 5 mV s^{-1} , (e) GCD curves at a current density of 0.5 mA cm^{-2} , and (f) the corresponding calculated gravimetric capacitances of the PyrCMO-5 mM hybrid electrode measured in different electrolyte solutions. (g) CV curves at different scan rates, (h) GCD curves, and (i) gravimetric and geometric capacitances of the PyrCMO-5 mM electrode at different current densities in a 1 M H_2SO_4 solution.

in Figure 4e, the peaks at 1590 and 1360 cm^{-1} , observed for both the PyrC and PyrCMO samples, correspond to crystalline graphite (G band) and disordered carbon (D band), respectively. The in-plane crystallite size (L_a), which represents the graphitic microcrystalline domain size, is empirically known to be inversely proportional to the D and G peak intensity ratio [i.e., $L_a \propto 1/(I_D/I_G)$].^{49,50} The PyrCMO sample shows a slightly higher I_D/I_G ratio (1.05) than the PyrC electrode (0.97), which might be due to a lower fraction of graphitic microcrystalline domains and/or the formation of more disorder or defects in the carbon during the pyrolysis process in the presence of MnO_2 nanostructures.^{51–53} This could be ascribed to the chemical reduction of the MnO_4 ions on the surface of the 3D-printed polymer precursor structure during the metal oxide synthesis process, which might change the surface chemistry and surface packing density and form structural defects in the polymer network.⁵¹ Furthermore, the Raman spectrum of PyrCMO shows peaks at 655 , 361 , and 316 cm^{-1} corresponding to the A_{1g} , T_{2g} , and E_g symmetric vibration modes, respectively. These are typical Raman peaks for crystalline hausmannite- Mn_3O_4 with a spinel structure,^{43,54} confirming the predominant presence of this oxide phase. EDS elemental mapping (Figure 4f) confirms that the manganese element is homogeneously distributed over the entire surface of the 3D carbon electrode.

Further investigation of the PyrCMO hybrid material was performed by TEM and HRTEM. Figure 5a shows a low-magnification TEM image of the PyrCMO hybrid material, which identifies that the Mn_3O_4 nanoparticles with different dimensions were distributed on the surface of the PyrC material. The single-crystal characteristics of the Mn_3O_4 nanoparticles are revealed in the HRTEM image and its corresponding fast Fourier transform (FFT; Figure 5b). It can be seen that the lattice fringes are arranged regularly with d spacings of 3.2 and 2.7 \AA , corresponding to the (101) and (211) planes of the tetragonal Mn_3O_4 crystals, respectively, consistent with the XRD patterns.^{15,55}

The electrochemical performance of the PyrCMO 3D hybrid material as SC electrodes was explored using a three-electrode cell and different aqueous electrolytes. For all of the PyrCMO electrodes synthesized with different MnO_x precursor concentrations (0–10 mM), the CV (Figure 6a) and GCD (Figure 6b) curves exhibited quasi-rectangular and triangular shapes in a 2 M KCl electrolyte solution, respectively. It is also observed that the voltammetric currents and discharging times of the hybrid PyrCMO electrodes are significantly higher than those of the bare PyrC electrode. These parameters are directly proportional to the electrochemical capacitance, demonstrating that the incorporation of a nanostructured MnO_x layer on the surface of

the hierarchical 3D carbon electrode greatly enhanced the overall capacitance. The capacitance of the metal oxide layers mainly arises from (i) surface Faradaic reactions due to the adsorption/desorption of cations at the electrode/electrolyte interface and (ii) bulk Faradaic reactions due to the insertion/removal of cations in the bulk of the material in proximity to the electrode/electrolyte interface.^{20,25} The results showed that the voltammetric currents and discharging times of the PyrCMO electrodes increased as the metal oxide precursor concentration increased from 1.25 to 5 mM and then decreased slightly with a further increase of the precursor concentration. The initial increase with higher concentrations is correlated with a larger amount of MnO_x on the electrode, which was confirmed by SEM imaging. The observed decrease in the voltammetric current and discharging time for the PyrCMO-10 mM sample could be mainly ascribed to the poor intrinsic electrical conductivity of MnO_x as well as limitations for the diffusion and migration of ions within the thicker MnO_x layer.^{20,51,56} Moreover, the iR drop was found to gradually increase with an increase in the metal oxide precursor concentration (marked with arrows in Figure 6b). This observation could be attributed to deterioration of the electric contact among the MONPs and the 3D carbon structure with an increase in the amount of metal oxide deposition, which is also consistent with their poor intrinsic electrical conductivity.^{47,57}

Figure 6c shows the EIS results of the PyrC and PyrCMO electrodes fabricated with different metal oxide precursor concentrations in a 2 M KCl aqueous electrolyte. Moreover, the equivalent Randles circuit model employed for data fitting is represented in the inset of Figure 6c, and the results are summarized in Table S4. The Nyquist plots are roughly similar in shape, with a semicircle in the high-frequency region and a straight line in the low-frequency domain, illustrating the electrochemical stability of the synthesized electrodes in a large frequency range. It is noteworthy that the semicircle diameter, which corresponds to the charge-transfer resistance (R_{ct}), increases with an increase of the metal oxide precursor concentration. This validates the assumption of a poor intrinsic electrical conductivity of the MnO_x layer and its inhibitory effect on ion diffusion.⁵⁸ Altogether, considering the electrochemical performances, the PyrCMO-5 mM hybrid material was identified as the optimum electrode with the largest pseudocapacitive contribution to the overall capacitance and therefore chosen for further characterization.

In order to further evaluate the electrochemical capacitive performance of the PyrCMO hybrid electrode, CV tests at a scan rate of 5 mV s^{-1} and GCD measurements at the current density of 0.5 mA cm^{-2} (parts d and e of Figure 6, respectively) were conducted in different acidic (1 M H_2SO_4 and 1 M HClO_4), alkaline (6 M KOH), and neutral (1 M Na_2SO_4 and 2 M KCl) electrolytes. Because the optimal operating potential window of the PyrCMO hybrid electrode in the KOH electrolyte was found to be different from the other studied electrolytes, the CV and GCD curves measured in this electrolyte are shown in separate graphs (Figure S3). According to the GCD curves, the gravimetric specific capacitance C_g (F g^{-1}) of an electrode can be calculated as $C_g = I\Delta t/W\Delta V$, where I , Δt , W , and ΔV represent the discharge current (A), discharging duration (s), mass of the active material (i.e., the electrode's circular part, g), and potential window (V), respectively.

The specific gravimetric capacitances calculated from the GCD curves for the PyrCMO electrode in the above-mentioned electrolytes are shown in Figure 6f. In Figure 6d, a fast rise/decay

in the currents upon a change of the direction of the potential sweep is clearly identified, demonstrating that very fast and reversible Faradaic reactions occur between the PyrCMO electrode and all of the electrolytes. The higher voltammetric currents and longer discharging times in acidic solutions reveal that the PyrCMO hybrid electrode has a superior capacitive performance in these electrolytes. Most of the electrochemical capacitance arises from the absorption and/or insertion of cations at the electrode/electrolyte interface. Therefore, the improved capacitive performance attained for the acidic electrolytes could be ascribed to the smaller hydrated ion size and higher ionic conductivity of the H^+ cations (2.8 \AA and $350.1 \text{ S cm}^2 \text{ mol}^{-1}$, respectively) compared to the K^+ and Na^+ cations (3.31 \AA and $73.5 \text{ S cm}^2 \text{ mol}^{-1}$ and 3.58 \AA and $50.11 \text{ S cm}^2 \text{ mol}^{-1}$, respectively).⁵⁹ Moreover, to have an accurate comparison of the effect of acidic electrolytes on the electrochemical capacitance of the PyrCMO hybrid electrode, electrolytes with the same H^+ cation concentration (0.5 M H_2SO_4 compared with 1 M HClO_4) were evaluated, and the results are presented in Figure S4. As can be understood from the results, although the capacitance for 0.5 M H_2SO_4 is slightly lower than that for 1 M H_2SO_4 , it is still higher than the capacitance obtained in 1 M HClO_4 . The better electrochemical capacitive performance measured in a H_2SO_4 solution might be related to the considerably higher ionic conductivity of SO_4^{2-} anions ($160.0 \text{ S cm}^2 \text{ mol}^{-1}$) compared to that of ClO_4^- anions ($67.3 \text{ S cm}^2 \text{ mol}^{-1}$), which leads to higher mobility and transfer rate. It is worth mentioning that only a minor increase in the specific capacitance was observed with doubling of the concentration of a H_2SO_4 solution from 0.5 to 1 M. This might be due to the decrease in the distance between the ions at higher concentrations and thereby their repulsions, which could limit the diffusion rate of protons to the electrode/electrolyte interface.^{60,61}

In the past, very diverse capacitance values have been reported for Mn_3O_4 -based materials as SC electrodes. For instance, Dai et al. reported a specific capacitance of 133 F g^{-1} for spinel Mn_3O_4 -layered nanoarchitectures within an operational potential window of 0–0.9 V.³⁶ Dubal et al. reported specific capacitances of 284 F g^{-1} for a Mn_3O_4 thin film with triangular-shaped nanoparticles over a potential window of -0.1 to $+0.9 \text{ V}$ ⁶² and 398 F g^{-1} for vertically arranged stacked Mn_3O_4 nanosheets in the same potential window.³⁷ Li et al. reported 153 F g^{-1} for a Mn_3O_4 -anchored graphene sheet nanocomposite in the potential range from -0.1 to $+0.8 \text{ V}$.¹⁴ Wang et al. synthesized a porous graphene/ Mn_3O_4 nanocomposite with a specific capacitance of 208.3 F g^{-1} in the potential window of -0.2 to $+0.8 \text{ V}$.⁶³ Li et al. synthesized Mn_3O_4 nanoparticles via the hydrothermal method and showed a specific capacitance of 401 F g^{-1} in the potential range of 0–0.9 V.⁶⁴ It is important to note that, in almost all of the relevant reported studies, only the mass of active nanomaterials is used to calculate the specific gravimetric capacitance. However, in reality, the mass of the current collector, conductive agents, and polymer binder are also a part of the electrochemical capacitor electrodes and eventually should be considered. Therefore, to have more practical and realistic values, the specific capacitances in Figure 6 are calculated by considering the complete mass of the electrode including the carbon current collector and Mn_3O_4 nanomaterials. A specific gravimetric capacitance of 186 F g^{-1} is obtained for the PyrCMO hybrid electrode at a current density of 0.5 mA cm^{-2} in the 1 M H_2SO_4 electrolyte. Additionally, for a fair comparison of the capacitance value with the state-of-the-art

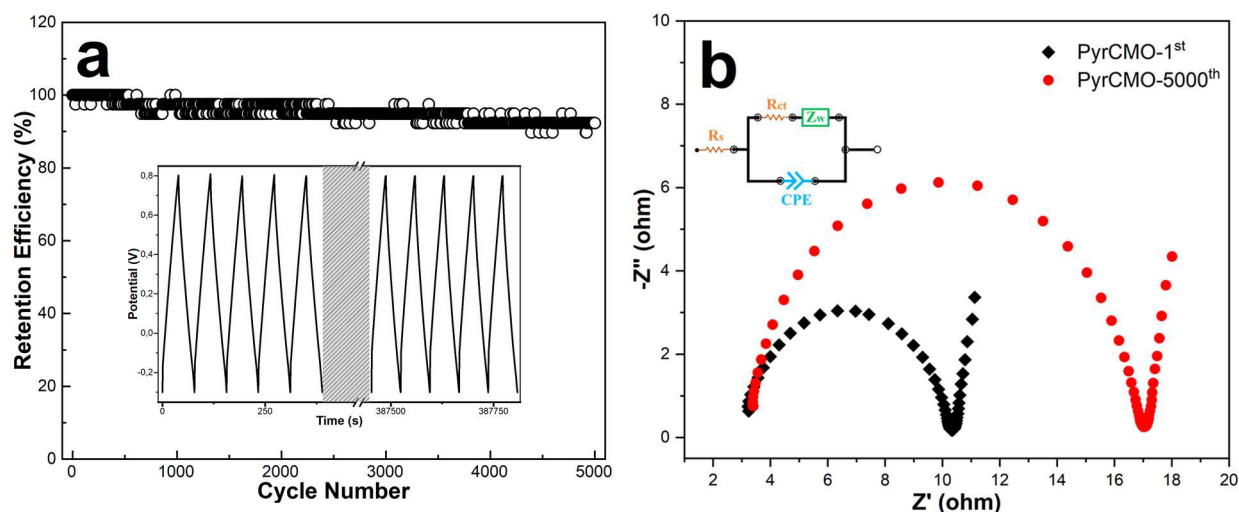


Figure 7. (a) Cycling performance of the PyrCMO hybrid electrode at a current density of 10 mA cm^{-2} in a $1 \text{ M H}_2\text{SO}_4$ solution as the electrolyte. The inset shows the first and last five charge–discharge curves. (b) Nyquist plots of the PyrCMO electrode before and after a 5000 cycling test in a $1 \text{ M H}_2\text{SO}_4$ solution.

Mn_3O_4 -based SC electrodes discussed above, the specific gravimetric capacitance value was recalculated considering only the mass of an active pseudocapacitive material using eq 1:²⁵

$$C_m = \frac{I_A(\Delta t_{\text{PyrCMO}} - \Delta t_C)}{\Delta V m_{\text{Mn}_3\text{O}_4}} \quad (1)$$

where $m_{\text{Mn}_3\text{O}_4}$ is the mass of a Mn_3O_4 thin layer decorated on the surface of the 3D carbon current collector, Δt_{PyrCMO} and Δt_C are the discharging times of the PyrCMO and PyrC electrodes, respectively, and ΔV is the operational potential window. The mass of the MnO_x nanostructures was estimated by subtracting the mass of the electrode after dissolving the metal oxide thin layer from the total mass of the electrode before dissolution. Dissolution of the MnO_x thin layer was carried out by soaking the electrode at least three times in 2 mL of a freshly prepared solution of hydrochloric acid (5 wt %) and hydrogen peroxide (5 wt %) under vacuum for 8 h each time.⁶⁵ The leaching process was repeated until no weight change in the dried electrode was observed. The resulting specific gravimetric capacitance of about 457 F g^{-1} at a current density of 0.5 mA cm^{-2} is comparable with those of state-of-the-art SC electrodes.^{13,14,35,37,66–69}

The PyrCMO hybrid electrode exhibited an ideal rate performance, which can be concluded based on quasi-rectangular CV curves at different scan rates (Figure 6g) and maintenance of the symmetric triangular GCD shapes at different current densities (Figure 6h). The slight deformation of CV curves at high scan rates of 50 and 100 mV s^{-1} might be attributed to the kinetically slow pseudocapacitive reactions and diffusion-limited charge-transfer processes within the MnO_x layer.²⁵ The specific gravimetric and geometric capacitance values were calculated and plotted as a function of the current density in Figure 6i. At a low current density, diffusion of ions through a porous electrode is facilitated, typically resulting in a higher specific capacitance. Contrarily, when the current density is high, the effective utilization of the electrode materials is mainly confined to the outer surface layers, leading to a lower specific capacitance. The PyrCMO electrodes overall followed this behavior typical for porous electrodes. However, Figure 6i shows that, despite a 10-fold increase of the current density from

0.5 to 5 mA cm^{-2} , around 60% of the initial specific capacitance was still retained. This implies that the PyrCMO hybrid electrode has a good rate capability and electrochemical reversibility, which are very crucial material properties to provide sufficient power density in SCs.

The long-term cycling performance of the 3D PyrCMO hybrid electrode was evaluated by repeating the GCD measurements at 10 mA cm^{-2} for 5000 continuous cycles. As shown in Figure 7a, almost 92.3% of its capacitance is retained after 5000 cycles, indicating that the integrity of the MnO_x layer and 3D carbon electrode is stable and well-preserved after long-term operation. Nyquist plots of the optimized PyrCMO hybrid electrode before and after cyclic stability testing in a $1 \text{ M H}_2\text{SO}_4$ electrolyte solution are shown in Figure 7b, and the results are summarized in Table S5. The intercept of the EIS curve and the real resistance (Z') in the high-frequency region corresponds to the combined resistance R_s of the (i) ionic resistance of the electrolyte, (ii) intrinsic resistance of the substrate, and (iii) electrode material/current collector contact resistance. This value is almost identical for the PyrCMO hybrid electrode before and after successive charge–discharge cycling, which means that the intrinsic ohmic resistance of the supercapacitive materials is well-preserved even after long-term operation. The major differences are the diameters of the semicircles, corresponding to R_{ct} caused by Faradaic reactions and the double-layer capacitance at the electrode/electrolyte interface.⁵¹ The calculated R_{ct} for the PyrCMO hybrid electrode increased after 5000 charge–discharge cycles. Increasing the R_{ct} for the PyrCMO hybrid electrode after 5000 charge–discharge cycles while almost 92.3% of its capacitance is retained might be ascribed to the gradual activation and increasing accessibility of ions into the porous Mn_3O_4 layer during long-term cycling, which has compensated the loss of adhesion of some pseudocapacitive materials with the 3D carbon sublayer.⁷⁰

4. CONCLUSIONS

In summary, a novel free-standing and binder-free 3D hybrid SC material with complex carbon architecture and metal oxide nanomaterials was fabricated using a simple and tailorable method. The most salient and distinctive features of the developed approach are (i) the flexibility to tailor the design and

fabricate on-demand and customized 3D electrode architectures, (ii) the *in situ* self-assembly of MnO₂ nanostructures directly on the polymer precursor, providing excellent integrity of the pseudocapacitive nanomaterials and the 3D PyrC electrode after thermal treatment, (iii) the simplicity and accessibility of the fabrication process combining simultaneous pyrolysis of the polymer precursor and annealing of a manganese oxide nanostructured layer in one single thermal processing step, and (IV) mass production capability. The method resulted in predominant decoration of 3D PyrC with crystalline Mn₃O₄ nanoparticles, which is one of the most preferred materials for electrochemical capacitive energy storage.

The electrochemical performance of the novel hybrid SC electrodes developed in this research is comparable to values reported in other studies. The results clearly reveal the potential capability of the 3D PyrCMO hybrid SC materials developed to meet the requirements for architectural tailorability, good capacitance (gravimetric and areal capacitances of 186 F g⁻¹ and 968 mF cm⁻², respectively) and rate capability, and a long cycling life of up to 5000 times (less than 8% loss), which are crucial parameters for high-performance EES devices. If solely the mass of the active MnO_x nanomaterial is considered, the gravimetric capacitance is 457 F g⁻¹, which is comparable to the values for state-of-the-art materials reported in the literature.

■ ASSOCIATED CONTENT

SI Supporting Information

The Supporting Information is available free of charge at <https://pubs.acs.org/doi/10.1021/acsnm.1c03251>.

Summary of the physicochemical properties of the commercial photopolymer utilized in this study, provided by the manufacturer (Table S1), XPS survey spectra and high-resolution spectra of the C 1s region of the 3D-printed HTR before and after oxygen plasma treatment (Figure S1), surface atomic composition of the 3D-printed HTR before and after oxygen plasma treatment (Table S2), surface atomic composition of the 3D-printed HTR and HTR/MnO_x hybrid materials with different precursor concentrations before and after the pyrolysis/annealing process (Table S3), XPS survey spectra of the 3D HTRMO hybrid materials and XPS core-level spectra of Mn 3s (Figure S2), electrochemical parameters obtained from the EIS data for 3D PyrC and PyrCMO hybrid electrodes (Table S4), CV and GCD curves of an optimum PyrCMO hybrid electrode in a 6 M KOH aqueous solution electrolyte (Figure S3), CV and discharging curves of the PyrCMO-5 mM hybrid electrode measured in 1 M H₂SO₄, 1 M HClO₄, and 0.5 M H₂SO₄ aqueous electrolyte solutions (Figure S4), and electrochemical parameters obtained from the EIS data before and after 5000 cycling test (Table S5) (PDF)

■ AUTHOR INFORMATION

Corresponding Author

Stephan Sylvest Keller – National Centre for Nano Fabrication and Characterization, DTU Nanolab, Technical University of Denmark, 2800 Kongens Lyngby, Denmark; Email: suke@dtu.dk

Authors

Babak Rezaei – National Centre for Nano Fabrication and Characterization, DTU Nanolab, Technical University of

Denmark, 2800 Kongens Lyngby, Denmark; orcid.org/0000-0002-8177-5363

Thomas Willum Hansen – National Centre for Nano Fabrication and Characterization, DTU Nanolab, Technical University of Denmark, 2800 Kongens Lyngby, Denmark

Complete contact information is available at:

<https://pubs.acs.org/10.1021/acsnm.1c03251>

Author Contributions

B.R.: data curation, formal analysis, investigation, methodology, validation, visualization, writing the original draft, writing the review, and editing. T.W.H.: data curation, formal analysis, writing the review, and editing. S.S.K.: project administration, resources, supervision, writing the review, and editing. All authors have given approval to the final version of the manuscript.

Notes

The authors declare no competing financial interest.

■ ACKNOWLEDGMENTS

B.R. is thankful for H. C. Ørsted Cofund for funding. This work was financially supported by the European Research Council under the Horizon 2020 framework programme (Grant 772370-PHOENEX).

■ REFERENCES

- (1) Wang, K.; Wang, S.; Liu, J.; Guo, Y.; Mao, F.; Wu, H.; Zhang, Q. Fe-Based Coordination Polymers as Battery-Type Electrodes in Semi-Solid-State Battery-Supercapacitor Hybrid Devices. *ACS Appl. Mater. Interfaces* **2021**, *13* (13), 15315–15323.
- (2) Wang, K.; Wang, Z.; Liu, J.; Li, C.; Mao, F.; Wu, H.; Zhang, Q. Enhancing the Performance of a Battery-Supercapacitor Hybrid Energy Device through Narrowing the Capacitance Difference between Two Electrodes via the Utilization of 2D MOF-Nanosheet-Derived Ni@ Nitrogen-Doped-Carbon Core-Shell Rings as Both Negative and P. *ACS Appl. Mater. Interfaces* **2020**, *12* (42), 47482–47489.
- (3) El-Kady, M. F.; Ihns, M.; Li, M.; Hwang, J. Y.; Mousavi, M. F.; Chaney, L.; Lech, A. T.; Kaner, R. B. Engineering Three-Dimensional Hybrid Supercapacitors and Microsupercapacitors for High-Performance Integrated Energy Storage. *Proc. Natl. Acad. Sci. U. S. A.* **2015**, *112* (14), 4233–4238.
- (4) Zhang, S.; Pan, N. Supercapacitors Performance Evaluation. *Adv. Energy Mater.* **2015**, *5* (6), 1401401.
- (5) Zhao, C.; Wang, C.; Gorkin, R.; Beirne, S.; Shu, K.; Wallace, G. G. Three Dimensional (3D) Printed Electrodes for Interdigitated Supercapacitors. *Electrochem. Commun.* **2014**, *41*, 20–23.
- (6) Subramani, K.; Sudhan, N.; Divya, R.; Sathish, M. All-Solid-State Asymmetric Supercapacitors Based on Cobalt Hexacyanoferrate-Derived CoS and Activated Carbon. *RSC Adv.* **2017**, *7* (11), 6648–6659.
- (7) Iro, Z. S.; Subramani, C.; Dash, S. S. A Brief Review on Electrode Materials for Supercapacitor. *Int. J. Electrochem. Sci.* **2016**, *11* (12), 10628–10643.
- (8) Jiang, H.; Li, C.; Sun, T.; Ma, J. A Green and High Energy Density Asymmetric Supercapacitor Based on Ultrathin MnO₂ Nanostructures and Functional Mesoporous Carbon Nanotube Electrodes. *Nanoscale* **2012**, *4* (3), 807–812.
- (9) Beidaghi, M.; Wang, C. Micro-Supercapacitors Based on Three Dimensional Interdigital Polypyrrole/C-MEMS Electrodes. *Electrochim. Acta* **2011**, *56* (25), 9508–9514.
- (10) Tsai, Y. C.; Yang, W. D.; Lee, K. C.; Huang, C. M. An Effective Electrodeposition Mode for Porous MnO₂/Ni Foam Composite for Asymmetric Supercapacitors. *Materials* **2016**, *9* (4), 246.
- (11) Jiang, Y.; Liu, J. Definitions of Pseudocapacitive Materials: A Brief Review. *Energy Environ. Mater.* **2019**, *2* (1), 30–37.

- (12) Hosseini, M. G.; Shahryari, E. Synthesis, Characterization and Electrochemical Study of Graphene Oxide-Multi Walled Carbon Nanotube-Manganese Oxide-Polyaniline Electrode as Supercapacitor. *J. Mater. Sci. Technol.* **2016**, *32* (8), 763–773.
- (13) Dubal, D. P.; Dhawale, D. S.; Salunkhe, R. R.; Pawar, S. M.; Lokhande, C. D. A Novel Chemical Synthesis and Characterization of Mn₃O₄ Thin Films for Supercapacitor Application. *Appl. Surf. Sci.* **2010**, *256* (14), 4411–4416.
- (14) Li, L.; Seng, K. H.; Liu, H.; Nevirkovets, I. P.; Guo, Z. Synthesis of Mn₃O₄-Anchored Graphene Sheet Nanocomposites via a Facile, Fast Microwave Hydrothermal Method and Their Supercapacitive Behavior. *Electrochim. Acta* **2013**, *87*, 801–808.
- (15) Wu, Y.; Liu, S.; Wang, H.; Wang, X.; Zhang, X.; Jin, G. A Novel Solvothermal Synthesis of Mn₃O₄/Graphene Composites for Supercapacitors. *Electrochim. Acta* **2013**, *90*, 210–218.
- (16) Yadav, A. A.; Jadhav, S. N.; Chougule, D. M.; Patil, P. D.; Chavan, U. J.; Kolekar, Y. D. Spray Deposited Hausmannite Mn₃O₄ Thin Films Using Aqueous/Organic Solvent Mixture for Supercapacitor Applications. *Electrochim. Acta* **2016**, *206*, 134–142.
- (17) Jao, P. F.; Kim, K. T.; Kim, G. J.-A.; Yoon, Y.-K. Fabrication of an All SU-8 Electrospun Nanofiber Based Supercapacitor. *J. Micromech. Microeng.* **2013**, *23* (11), 114011.
- (18) Zhang, P.; Li, K.; Liu, X. Carnation-like MnO₂ Modified Activated Carbon Air Cathode Improve Power Generation in Microbial Fuel Cells. *J. Power Sources* **2014**, *264*, 248–253.
- (19) Wang, X.; Myers, B. D.; Yan, J.; Shekhawat, G.; Dravid, V.; Lee, P. S. Manganese Oxide Micro-Supercapacitors with Ultra-High Areal Capacitance. *Nanoscale* **2013**, *5* (10), 4119–4122.
- (20) Barai, H. R.; Banerjee, A. N.; Hamnabard, N.; Joo, S. W. Synthesis of Amorphous Manganese Oxide Nanoparticles-to-Crystalline Nanorods through a Simple Wet-Chemical Technique Using K⁺ Ions as a “growth Director” and Their Morphology-Controlled High Performance Supercapacitor Applications. *RSC Adv.* **2016**, *6* (82), 78887–78908.
- (21) Acharyya, D.; Ghosal, S.; Roychoudhuri, R.; Bhattacharyya, P. Hierarchical MnO₂ Nanoflowers Based Efficient Room Temperature Alcohol Sensor. *Proc. IEEE Sensors* **2018**, *2018* (October), 1–4.
- (22) Jiang, S.; Shi, T.; Gao, Y.; Long, H.; Xi, S.; Tang, Z. Fabrication of a 3D Micro/Nano Dual-Scale Carbon Array and Its Demonstration as the Microelectrodes for Supercapacitors. *J. Micromech. Microeng.* **2014**, *24* (4), 045001.
- (23) Beidaghi, M.; Gogotsi, Y. Capacitive Energy Storage in Micro-Scale Devices: Recent Advances in Design and Fabrication of Micro-Supercapacitors. *Energy Environ. Sci.* **2014**, *7* (3), 867.
- (24) Agrawal, R.; Adelowo, E.; Baboukani, A.; Villegas, M.; Henriques, A.; Wang, C. Electrostatic Spray Deposition-Based Manganese Oxide Films—From Pseudocapacitive Charge Storage Materials to Three-Dimensional Microelectrode Integrand. *Nanomaterials* **2017**, *7* (8), 198.
- (25) Jiang, S.; Shi, T.; Liu, D.; Long, H.; Xi, S.; Wu, F.; Li, X.; Xia, Q.; Tang, Z. Integration of MnO₂ Thin Film and Carbon Nanotubes to Three-Dimensional Carbon Microelectrodes for Electrochemical Microcapacitors. *J. Power Sources* **2014**, *262*, 494–500.
- (26) De Volder, M.; Hart, A. J. Engineering Hierarchical Nanostructures by Elastocapillary Self-Assembly. *Angew. Chem., Int. Ed.* **2013**, *52* (9), 2412–2425.
- (27) Chamran, F.; Yeh, Y.; Min, H. S.; Dunn, B.; Kim, C. J. Fabrication of High-Aspect-Ratio Electrode Arrays for Three-Dimensional Microbatteries. *J. Microelectromech. Syst.* **2007**, *16* (4), 844–852.
- (28) Qi, Z.; Ye, J.; Chen, W.; Biener, J.; Duoss, E. B.; Spadaccini, C. M.; Worsley, M. A.; Zhu, C. 3D-Printed, Superelastic Polypyrrole-Graphene Electrodes with Ultrahigh Areal Capacitance for Electrochemical Energy Storage. *Adv. Mater. Technol.* **2018**, *3* (7), 1800053.
- (29) Song, S.; Park, M.; Lee, J.; Yun, J. A Study on the Rheological and Mechanical Properties of Photo-Curable Ceramic/Polymer Composites with Different Silane Coupling Agents for SLA 3D Printing Technology. *Nanomaterials* **2018**, *8* (2), 93.
- (30) Rezaei, B.; Pan, J. Y.; Gundlach, C.; Keller, S. S. Highly Structured 3D Pyrolytic Carbon Electrodes Derived from Additive Manufacturing Technology. *Mater. Des.* **2020**, *193*, 108834.
- (31) Sukhdev, A.; Challa, M.; Narayani, L.; Manjunatha, A. S.; Deepthi, P. R.; Angadi, J. V.; Mohan Kumar, P.; Pasha, M. Synthesis, Phase Transformation, and Morphology of Hausmannite Mn₃O₄ Nanoparticles: Photocatalytic and Antibacterial Investigations. *Heliyon* **2020**, *6* (1), No. e03245.
- (32) Vesali-Naseh, M.; Khodadadi, A. A.; Mortazavi, Y.; Moosavi-Movahedi, A. A.; Ostrikov, K. H. ₂O/Air Plasma-Functionalized Carbon Nanotubes Decorated with MnO₂ for Glucose Sensing. *RSC Adv.* **2016**, *6* (38), 31807–31815.
- (33) Mendez-Linan, J. I.; Ortiz-Ortega, E.; Jimenez-Moreno, M. F.; Mendivil-Palma, M. I.; Martínez-Guerra, E.; Aguirre-Tostado, F. S.; Martínez-Chapa, S. O.; Hosseini, S.; Madou, M. J. Aging Effect of Plasma-Treated Carbon Surfaces: An Overlooked Phenomenon. *Carbon* **2020**, *169*, 32–44.
- (34) Lee, J. W.; Hall, A. S.; Kim, J.-D.; Mallouk, T. E. A Facile and Template-Free Hydrothermal Synthesis of Mn₃O₄ Nanorods on Graphene Sheets for Supercapacitor Electrodes with Long Cycle Stability. *Chem. Mater.* **2012**, *24* (6), 1158–1164.
- (35) Hu, Y.; Wang, J. MnOx Nanosheets for Improved Electrochemical Performances through Bilayer Nano-Architecting. *J. Power Sources* **2015**, *286*, 394–399.
- (36) Dai, Y.; Wang, K.; Xie, J. From Spinel Mn₃O₄ to Layered Nanoarchitectures Using Electrochemical Cycling and the Distinctive Pseudocapacitive Behavior. *Appl. Phys. Lett.* **2007**, *90* (10), 104102.
- (37) Dubal, D. P.; Holze, R. Self-Assembly of Stacked Layers of Mn₃O₄ Nanosheets Using a Scalable Chemical Strategy for Enhanced, Flexible, Electrochemical Energy Storage. *J. Power Sources* **2013**, *238*, 274–282.
- (38) Ullah, A. K. M. A.; Kibria, A. K. M. F.; Akter, M.; Khan, M. N. I.; Maksud, M. A.; Jahan, R. A.; Firoz, S. H. Synthesis of Mn₃O₄ Nanoparticles via a Facile Gel Formation Route and Study of Their Phase and Structural Transformation with Distinct Surface Morphology upon Heat Treatment. *J. Saudi Chem. Soc.* **2017**, *21* (7), 830–836.
- (39) Zhao, S.; Liu, T.; Hou, D.; Zeng, W.; Miao, B.; Hussain, S.; Peng, X.; Javed, M. S. Controlled Synthesis of Hierarchical Birnessite-Type MnO₂ Nanoflowers for Supercapacitor Applications. *Appl. Surf. Sci.* **2015**, *356*, 259–265.
- (40) Weng, X.; Long, Y.; Wang, W.; Shao, M.; Wu, Z. Structural Effect and Reaction Mechanism of MnO₂ Catalysts in the Catalytic Oxidation of Chlorinated Aromatics. *Chin. J. Catal.* **2019**, *40* (5), 638–646.
- (41) Islam, M.; Flach, J.; Martinez-Duarte, R. Carbon Origami: A Method to Fabricate Lightweight Carbon Cellular Materials. *Carbon* **2018**, *133*, 140–149.
- (42) Li, Y.; Mu, L.; Hu, Y.-S.; Li, H.; Chen, L.; Huang, X. Pitch-Derived Amorphous Carbon as High Performance Anode for Sodium-Ion Batteries. *Energy Storage Mater.* **2016**, *2*, 139–145.
- (43) Narayani, L.; Jagadeesha Angadi, V.; Sukhdev, A.; Challa, M.; Mattepanavar, S.; Deepthi, P. R.; Mohan Kumar, P.; Pasha, M. Mechanism of High Temperature Induced Phase Transformation and Magnetic Properties of Mn₃O₄ Crystallites. *J. Magn. Magn. Mater.* **2019**, *476*, 268–273.
- (44) Wang, J.; Zeng, R.; Du, G.; Li, W.; Chen, Z.; Li, S.; Guo, Z.; Dou, S. Rapid Microwave-Assisted Synthesis of Various MnO₂ Nanostructures and Their Magnetic Properties. *Mater. Chem. Phys.* **2015**, *166*, 42–48.
- (45) Wang, X.; Li, Y. Synthesis and Formation Mechanism of Manganese Dioxide Nanowires/Nanorods. *Chem. - Eur. J.* **2003**, *9* (1), 300–306.
- (46) Luo, J.; Zhu, H.; Fan, H.; Liang, J.; Shi, H.; Rao, G.; Li, J.; Du, Z.; Shen, Z. Synthesis of Single-Crystal Tetragonal α -MnO₂ Nanotubes. *J. Phys. Chem. C* **2008**, *112*, 12594–12598.
- (47) Huang, Y.; Li, Y.; Hu, Z.; Wei, G.; Guo, J.; Liu, J. A Carbon Modified MnO₂ Nanosheet Array as a Stable High-Capacitance Supercapacitor Electrode. *J. Mater. Chem. A* **2013**, *1* (34), 9809.
- (48) Yang, P.; Ding, Y.; Lin, Z.; Chen, Z.; Li, Y.; Qiang, P.; Ebrahimi, M.; Mai, W.; Wong, C. P.; Wang, Z. L. Low-Cost High-Performance

Solid-State Asymmetric Supercapacitors Based on MnO₂nanowires and Fe₂O₃Nanotubes. *Nano Lett.* **2014**, *14* (2), 731–736.

(49) McCreery, R. L. Advanced Carbon Electrode Materials for Molecular Electrochemistry. *Chem. Rev.* **2008**, *108* (7), 2646–2687.

(50) Maitra, T.; Sharma, S.; Srivastava, A.; Cho, Y. K.; Madou, M.; Sharma, A. Improved Graphitization and Electrical Conductivity of Suspended Carbon Nanofibers Derived from Carbon Nanotube/Polyacrylonitrile Composites by Directed Electrospinning. *Carbon* **2012**, *50* (5), 1753–1761.

(51) Yan, J.; Fan, Z.; Wei, T.; Qian, W.; Zhang, M.; Wei, F. Fast and Reversible Surface Redox Reaction of Graphene–MnO₂ Composites as Supercapacitor Electrodes. *Carbon* **2010**, *48* (13), 3825–3833.

(52) Caçado, L. G.; Pimenta, M. A.; Neves, B. R. A.; Dantas, M. S. S.; Jorio, A. Influence of the Atomic Structure on the Raman Spectra of Graphite Edges. *Phys. Rev. Lett.* **2004**, *93* (24), 247401.

(53) Xie, Q.; Chen, G.; Bao, R.; Zhang, Y.; Wu, S. Polystyrene Foam Derived Nitrogen-Enriched Porous Carbon/Graphene Composites with High Volumetric Capacitances for Aqueous Supercapacitors. *Microporous Mesoporous Mater.* **2017**, *239*, 130–137.

(54) Tian, Z. Y.; Mountapmbeme Kouotou, P.; Bahlawane, N.; Tchoua Ngamou, P. H. Synthesis of the Catalytically Active Mn₃O₄ Spinel and Its Thermal Properties. *J. Phys. Chem. C* **2013**, *117* (12), 6218–6224.

(55) Cheng, Y.; Wei, Z.; Du, Q.; Liu, F.; Duan, X.; Wang, Y.; Jia, D.; Zhou, Y.; Li, B. The Shape Effect of Manganese(II,III) Oxide Nanoparticles on the Performance of Electrochemical Capacitors. *Electrochim. Acta* **2018**, *284*, 408–417.

(56) Fischer, A. E.; Pettigrew, K. A.; Rolison, D. R.; Stroud, R. M.; Long, J. W. Incorporation of Homogeneous, Nanoscale MnO₂ within Ultraporos Carbon Structures via Self-Limiting Electroless Deposition: Implications for Electrochemical Capacitors. *Nano Lett.* **2007**, *7* (2), 281–286.

(57) Cheng, Y.; Wei, Z.; Du, Q.; Liu, F.; Duan, X.; Wang, Y.; Jia, D.; Zhou, Y.; Li, B. The Shape Effect of Manganese(II,III) Oxide Nanoparticles on the Performance of Electrochemical Capacitors. *Electrochim. Acta* **2018**, *284*, 408–417.

(58) Chen, W.; Rakhi, R. B.; Hu, L.; Xie, X.; Cui, Y.; Alshareef, H. N. High-Performance Nanostructured Supercapacitors on a Sponge. *Nano Lett.* **2011**, *11* (12), 5165–5172.

(59) Zhong, C.; Deng, Y.; Hu, W.; Qiao, J.; Zhang, L.; Zhang, J. A Review of Electrolyte Materials and Compositions for Electrochemical Supercapacitors. *Chem. Soc. Rev.* **2015**, *44* (21), 7484–7539.

(60) Farma, R.; Deraman, M.; Talib, I. A.; Awitdrus; Omar, R.; Ishak, M. M.; Taer, E.; Basri, N. H.; Dolah, B. N. M. Effect of Electrolyte Concentration on Performance of Supercapacitor Carbon Electrode from Fibers of Oil Palm Empty Fruit Bunches. *AIP Conference Proceedings*; 2015; Vol. 1656, p 030006; DOI: 10.1063/1.4917095.

(61) Holla, S.; Selvakumar, M. Effect of Different Electrolytes on the Supercapacitor Behavior of Single and Multilayered Electrode Materials Based on Multiwalled Carbon Nanotube/Polyaniline Composite. *Macromol. Chem. Phys.* **2018**, *219* (21), 1800213.

(62) Dubal, D. P.; Dhawale, D. S.; Salunkhe, R. R.; Fulari, V. J.; Lokhande, C. D. Chemical Synthesis and Characterization of Mn₃O₄ Thin Films for Supercapacitor Application. *J. Alloys Compd.* **2010**, *497* (1–2), 166–170.

(63) Wang, T.; Le, Q.; Guo, X.; Huang, M.; Liu, X.; Dong, F.; Zhang, J.; Zhang, Y. X. Preparation of Porous Graphene@Mn₃O₄ and Its Application in the Oxygen Reduction Reaction and Supercapacitor. *ACS Sustainable Chem. Eng.* **2019**, *7* (1), 831–837.

(64) Li, B.; Zhang, X.; Dou, J.; Hu, C. Facile Synthesis of Pseudocapacitive Mn₃O₄ Nanoparticles for High-Performance Supercapacitor. *Ceram. Int.* **2019**, *45* (13), 16297–16304.

(65) Zeytuncu, B. Dissolution of Alkaline Batteries in Reductive Acidic Media. *Physicochem. Probl. Miner. Process.* **2016**, *52* (1), 437–450.

(66) Luo, Y.; Yang, T.; Li, Z.; Xiao, B.; Zhang, M. High Performance of Mn₃O₄ Cubes for Supercapacitor Applications. *Mater. Lett.* **2016**, *178*, 171–174.

(67) Dong, R.; Ye, Q.; Kuang, L.; Lu, X.; Zhang, Y.; Zhang, X.; Tan, G.; Wen, Y.; Wang, F. Enhanced Supercapacitor Performance of Mn₃O₄ Nanocrystals by Doping Transition-Metal Ions. *ACS Appl. Mater. Interfaces* **2013**, *5* (19), 9508–9516.

(68) Yu, M.; Zhai, T.; Lu, X.; Chen, X.; Xie, S.; Li, W.; Liang, C.; Zhao, W.; Zhang, L.; Tong, Y. Manganese Dioxide Nanorod Arrays on Carbon Fabric for Flexible Solid-State Supercapacitors. *J. Power Sources* **2013**, *239*, 64–71.

(69) Wang, K.; Shi, X.; Lu, A.; Ma, X.; Zhang, Z.; Lu, Y.; Wang, H. High Nitrogen-Doped Carbon/Mn₃O₄ Hybrids Synthesized from Nitrogen-Rich Coordination Polymer Particles as Supercapacitor Electrodes. *Dalt. Trans.* **2015**, *44* (1), 151–157.

(70) Li, L.; Hu, Z.; Yang, Y.; Liang, P.; Lu, A.; Xu, H.; Hu, Y.; Wu, H. Hydrothermal Self-Assembly Synthesis of Mn₃O₄/Reduced Graphene Oxide Hydrogel and Its High Electrochemical Performance for Supercapacitors. *Chin. J. Chem.* **2013**, *31* (10), 1290–1298.